

Article

Three-Dimensional Optical Spin Angular Momentum Flux of a Vector Beam with Radially-Variant Polarization in Near Field

Ying Guan ^{1,2}, Li-Xin Zhong ³, Chaoyang Qian ¹ and Rui-Pin Chen ^{1,*} 

¹ Key Laboratory of Optical Field Manipulation of Zhejiang Province, Department of Physics, Zhejiang Sci-Tech University, Hangzhou 310018, China; gying0423@163.com (Y.G.); qiacaoqyng@sngrowpower.cm (C.Q.)

² Zhejiang Provincial Key Laboratory of Chemical Utilization of Forestry Biomass, Zhejiang Agriculture and Forestry University, Hangzhou 311300, China

³ School of Finance, Zhejiang University of Finance and Economics, Hangzhou 310018, China; zlxwj@163.com

* Correspondence: chenrp@zstu.edu.cn; Tel.: +86-571-86843468

Received: 22 January 2019; Accepted: 5 March 2019; Published: 7 March 2019



Abstract: The near-field characteristics of a radially-variant vector beam (RVVB) are analyzed by using the vectorial angular spectrum method. The non-paraxial RVVB can be decomposed into the propagating wave and the evanescent wave in near field. The coherent superposition of the longitudinal and transverse components of the RVVB results in a three-dimensional (3D) profile of the spin angular momentum flux density (SAM-FD). The evanescent wave part dominates the near field of a highly non-paraxial RVVB. The longitudinal component has a large impact on the 3D shape of the optical SAM-FD. Therefore, the 3D SAM-FD configuration of the RVVB can be manipulated by choosing the initial states of polarization arrangement. In particular, the transverse SAM-FD with a spin axis orthogonal to the propagation direction offers a promising range of applications spanning from nanophotonics and plasmonics to biophotonics.

Keywords: vector beams; optical spin angular momentum; longitudinal component; radially-variant polarization

1. Introduction

The vector optical field with spatially-variant states of polarization (SoP) has been extensively studied because of the fundamental interest and novel characteristics it offers [1–6], such as focusing engineering [7,8], micro-particle manipulation [9,10], vectorial nonlinear optical collapse [11,12], and the optical spin-orbital angular momentum conversion in a highly non-paraxial vector beam [13]. For a highly non-paraxial vector beam, the evanescent wave [14,15] dominates the near field and the longitudinal component plays an important role in the evolution of the vector optical field. The quantitative knowledge of the near-field properties of an optical field is required in many applications ranging from nanophotonics to optical imaging [16–19]. Recently, the characteristics of the evanescent wave for a vector optical field with radial polarization and azimuthal polarization have been reported [20–22]. These works indicate that the longitudinal component of both the evanescent wave and the propagating wave can be manipulated by the initial SoP alignments. The study regarding the full vector structure of a highly non-paraxial vector beam has found many novel phenomena and applications. On the other hand, the three-dimensional (3D) vector structure of a highly non-paraxial vector beam may result in a 3D vector structure of the optical spin angular momentum flux density (SAM-FD) which is associated with the circular polarization [23,24]. In particular, the transverse

SAM-FD with a spin axis orthogonal to the propagation direction offers a promising range of applications spanning from nanophotonics and plasmonics to biophotonics.

In this paper, the radially-variant vector beam (RVVB) is split into the propagating wave and evanescent wave parts by using the angular spectrum method. A full vectorial description for the transverse and longitudinal components of a RVVB is presented. The profile of the longitudinal component is different from that of the transverse component. Both the longitudinal and transverse component profiles of the RVVB are closely related to the initial SoP arrangement. The coherent superposition of the longitudinal and transverse polarization components leads to the 3D SAM-FD profile. In particular, the longitudinal component dominates the near field in a highly non-paraxial RVVB. These results indicate that the 3D SAM-FD of a highly non-paraxial RVVB can be manipulated by the initial SoP in the beam cross-section.

2. Theoretical Formulation

We consider the RVVB propagation along the z-axis in the Cartesian coordinate system [1–3]:

$$E(r, \theta, z = 0) = A(r)[\exp(i2\pi(r/r_0)^2 + i\theta_0)e_x + \exp(-i2\pi(r/r_0)^2 + i\theta_0)e_y], \quad (1)$$

where $r = (x^2 + y^2)^{1/2}$ is the polar radius and $\theta = \arctan(y/x)$ is the azimuthal angle in the polar coordinate system. $A(r)$ denotes the amplitude of the RVVB, θ_0 is the initial phase, e_x and e_y are the x - and y -direction unit vectors. Figure 1 shows the initial SoP alignment in a Gaussian beam cross-section.

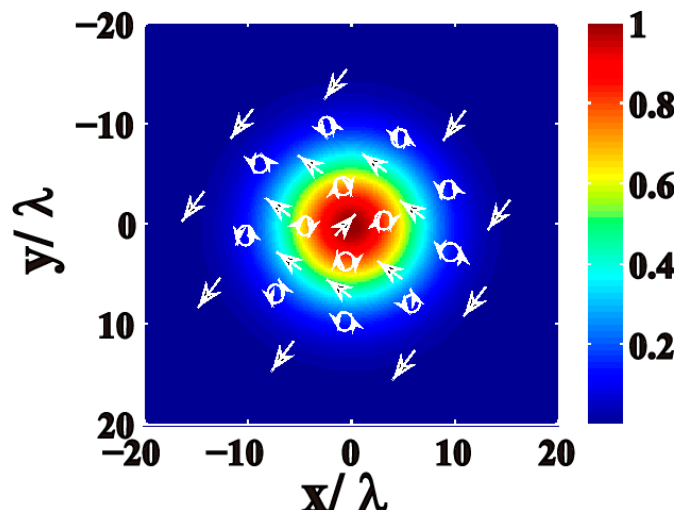


Figure 1. (Color online) The states of polarization (SoP) arrangement in the cross-sections of a radially-variant vector beam (RVVB) with a Gaussian amplitude. Here, λ is the wavelength.

By using the Fourier transform of the initial RVVB, the transverse components of the vector angular spectrum $A_x(\rho \cos \phi, \rho \sin \phi)$ and $A_y(\rho \cos \phi, \rho \sin \phi)$ can be given as [20–22]:

$$\begin{pmatrix} A_x(\rho \cos \phi, \rho \sin \phi) \\ A_y(\rho \cos \phi, \rho \sin \phi) \end{pmatrix} = \frac{k}{2\pi} \begin{pmatrix} \int_0^\infty \int_0^{2\pi} A(r) \exp[i2\pi(r/r_0)^2 + i\theta_0 - ik\rho \cos(\theta - \phi)] r d\theta dr \\ \int_0^\infty \int_0^{2\pi} A(r) \exp[-i2\pi(r/r_0)^2 + i\theta_0 - ik\rho \cos(\theta - \phi)] r d\theta dr \end{pmatrix}, \quad (2)$$

where ρ and ϕ are in relation with the transverse Fourier-transform variables μ, ν : $\mu = \rho \cos \phi, \nu = \rho \sin \phi$, and $\xi = (1 - \rho^2)^{1/2}$. k is the wavenumber. For the Gaussian beam $A(r) = \exp(-r^2/w^2)$ where w indicates the waist of Gaussian beam, the x, y , and z components of the angular spectrum of a RVVB (Equation (1)) are:

$$A_x(\rho \cos \phi, \rho \sin \phi) = \frac{k^2 r_0^2 w^2}{4\pi(r_0^2 - 2\pi w^2 i)} \exp\left(-\frac{k^2 \rho^2 r_0^2 w^2}{4r_0^2 - 8\pi w^2 i} + i\theta_0\right), \quad (3)$$

$$A_y(\rho \cos \phi, \rho \sin \phi) = \frac{k^2 r_0^2 w^2}{4\pi(r_0^2 + 2\pi w^2 i)} \exp\left(-\frac{k^2 \rho^2 r_0^2 w^2}{4r_0^2 + 8\pi w^2 i} + i\theta_0\right), \quad (4)$$

$$A_z(\rho \cos \phi, \rho \sin \phi) = \cos \phi A_x(\rho \cos \phi, \rho \sin \phi) + \sin \phi A_y(\rho \cos \phi, \rho \sin \phi). \quad (5)$$

The RVVB in the plane of propagation distance z can be calculated as [20–22]:

$$E(r, z) = \int_{-\infty}^{\infty} \int_{-\infty}^{\infty} A(\rho \cos \phi, \rho \sin \phi) \exp[ik(ux + vy + \xi z)] dudv. \quad (6)$$

Therefore, the x -, y - and z - components of the RVVB can be obtained by Equations (3)–(6):

$$E_x(r, z) = \frac{k^2 w^2 r_0^2 \exp(i\theta_0)}{2(r_0^2 - 2\pi w^2 i)} \int_0^{\infty} \exp\left[-\frac{k^2 \rho^2 r_0^2 w^2}{4r_0^2 - 8\pi w^2 i} + ik\sqrt{1 - \rho^2} z\right] J_0(rk\rho) \rho d\rho, \quad (7)$$

$$E_y(r, z) = \frac{k^2 w^2 r_0^2 \exp(i\theta_0)}{2(r_0^2 + 2\pi w^2 i)} \int_0^{\infty} \exp\left[-\frac{k^2 \rho^2 r_0^2 w^2}{4r_0^2 + 8\pi w^2 i} + ik\sqrt{1 - \rho^2} z\right] J_0(rk\rho) \rho d\rho, \quad (8)$$

$$E_z(r, z) = \frac{i k^2 w^2 r_0^2 \exp(i\theta_0)}{2} \left[\frac{\sin \theta}{r_0^2 - 2\pi w^2 i} \int_0^{\infty} \exp\left[-\frac{k^2 \rho^2 r_0^2 w^2}{4r_0^2 - 8\pi w^2 i} + ik\sqrt{1 - \rho^2} z\right] J_0(rk\rho) \rho d\rho \right. \\ \left. + \frac{\cos \theta}{r_0^2 + 2\pi w^2 i} \int_0^{\infty} \exp\left[-\frac{k^2 \rho^2 r_0^2 w^2}{4r_0^2 + 8\pi w^2 i} + ik\sqrt{1 - \rho^2} z\right] J_0(rk\rho) \rho d\rho \right]. \quad (9)$$

When the integrations are in the range: $1 \leq \rho < \infty$, they denote the evanescent wave component. On the other hand, if the integrations are in the region: $0 \leq \rho < 1$, they refer to the propagating wave component [20–22]. Furthermore, the corresponding SAM-FD of the RVVB can be given by [23,24]:

$$S_x = \varepsilon_0 \text{Im}(E_y E_z^*) / \omega,$$

$$S_y = \varepsilon_0 \text{Im}(E_x^* E_z) / \omega,$$

$$S_z = \varepsilon_0 \text{Im}(E_x E_y^*) / \omega,$$

where the asterisk denotes complex conjugation and $\text{Im}[\cdot]$ means taking the imaginary part. $S_{x,y,z}$ denote the x , y , and z components of the SAM-FD, ω is the angular frequency, ε_0 is permittivity in vacuum.

3. Numerical Results

The intensity patterns of different components of both the evanescent wave and the propagating wave are shown in Figures 2 and 3. The intensity patterns of x , y , and z components of the evanescent wave and propagation wave for different propagation distances are shown in Figure 2. Figure 3 shows the corresponding intensity patterns for different SoP arrangements with variant radial periods (i.e., different r_0 in this work).

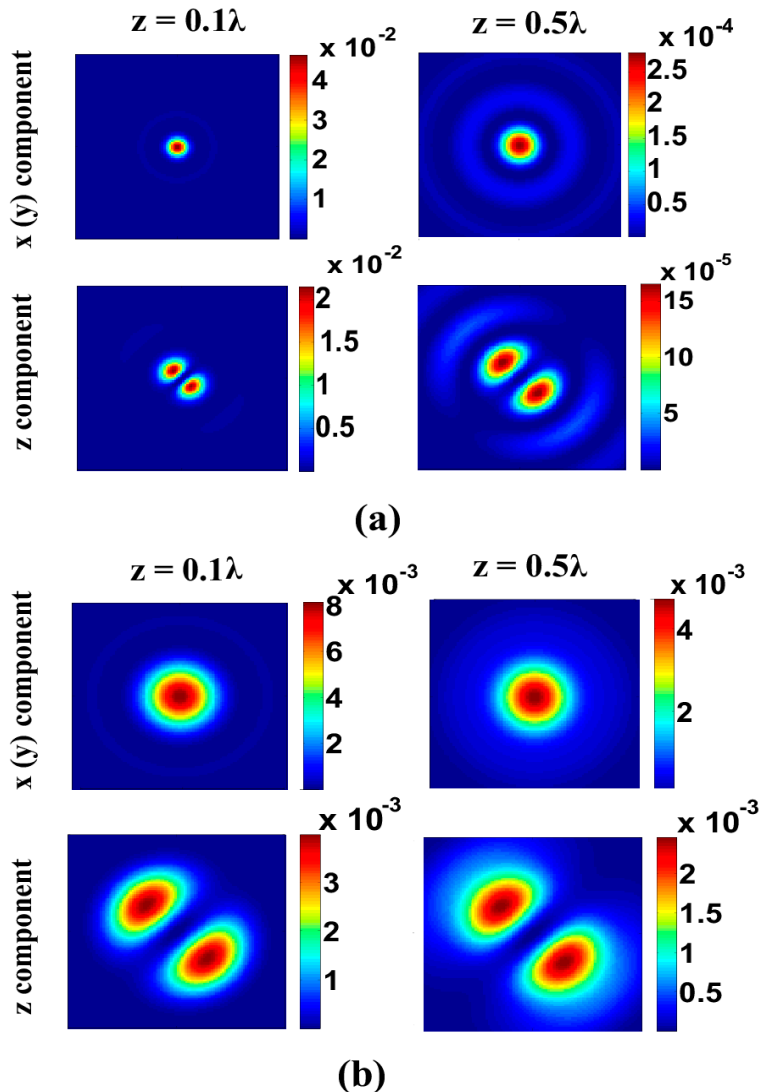


Figure 2. (Color online) Intensity patterns of x -, y - and z - components of the evanescent wave and propagating wave in the x - y plane for different propagation distances with $w = 0.1\lambda$, $r_0 = 0.5\lambda$: (a) the evanescent wave; (b) the propagating wave. Upper plots in (a,b) transverse (x or y) component; lower plots in (a,b) z component. All the images have the same dimension of $2 \times 2 \lambda^2$.

The evanescent wave part dominates the optical field in near field, and is closely related with the initial SoP alignment, as shown in Figures 2 and 3. The evanescent wave will spread out quickly and fade away with increasing propagation distance, as expected. The patterns of the longitudinal components are closely related to the initial SoP arrangements of the RVVB. In particular, the longitudinal components are not negligible in the near field that results in the variation of the total intensity patterns as shown in Figures 2 and 3. The patterns of the longitudinal component rotate with different radial periods of SoP arrangement (i.e., different r_0 in this work). Here, we would like to discuss the underlying physics of these phenomena. The radially variant polarization can be regarded as the superposition of the x - and y -polarization components with different initial phases, as recognized from Equation (1). The intensity patterns of the x and y components with different SoP are similar but different in phase, as recognized from Equations (7) and (8) and as shown in Figures 2 and 3. On the other hand, the different x - and y -component phases will contribute to the variation of the longitudinal component, as recognized from Equation (9). Therefore, the different SoP arrangements result in the different profiles of the longitudinal component, as shown in Figure 3. The manipulation of the longitudinal component shapes [25,26] has become an essential approach

because of the fundamental physics and the potential applications for super-resolution, plasmonic beaming, nanofabrication, and 3D imaging, etc. Obviously, these results indicate the longitudinal component patterns can be controlled by the initial SoP arrangement using the above analysis.

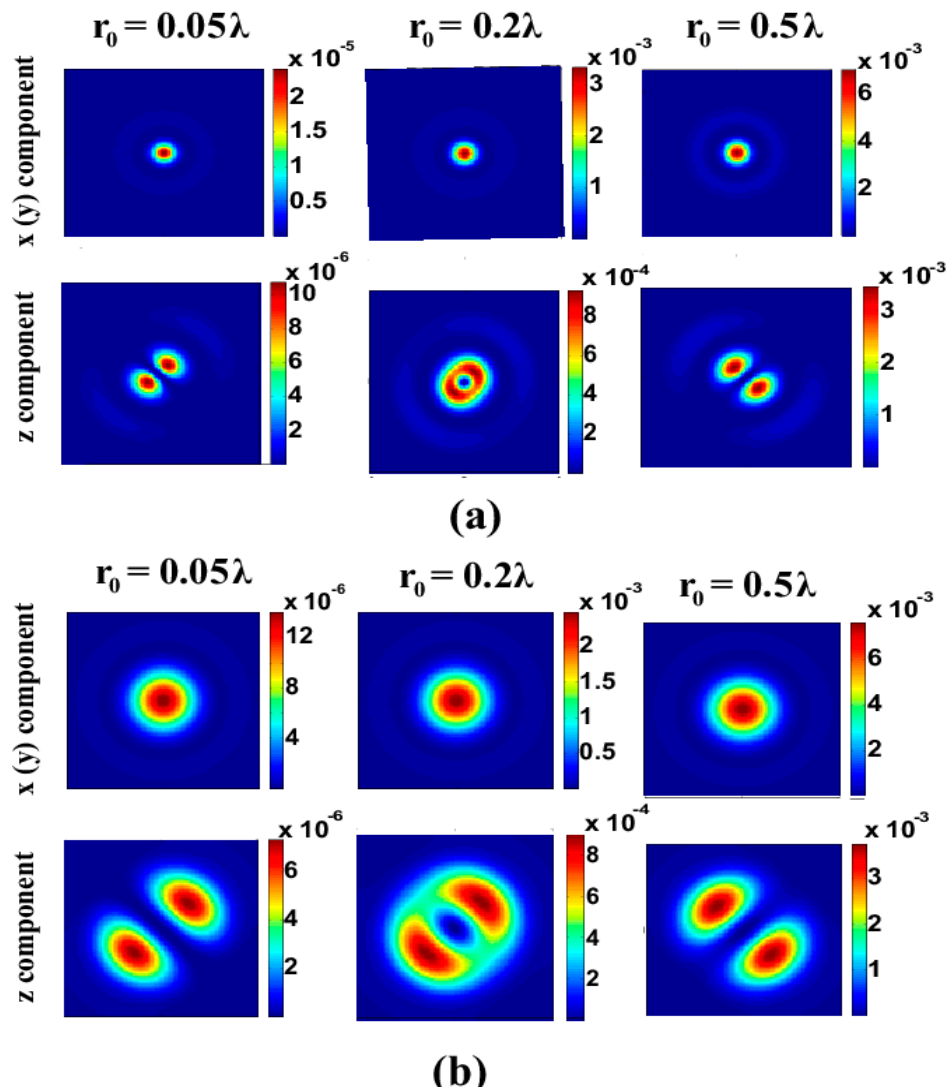


Figure 3. (Color online) Intensity patterns of x -, y - and z -components with different radial periods of initial SoP alignments (i.e., different r_0 in this work) and $w = 0.1\lambda$: (a) the evanescent wave; (b) the propagation wave. Upper plots in (a,b) transverse (x or y) component; lower plots in (a,b) z component. All the images have the same dimension of $2 \times 2 \lambda^2$.

It is interesting to examine the evolution of the optical SAM-FD in the near field with different SoP arrangements. In particular, the longitudinal component of a vector beam cannot be neglected in the near field, which results in the transverse components of the optical SAM-FD (i.e., S_x , S_y). The 3D SAM-FD paves a new way for potential applications in the corresponding fields such as manipulation of micro-particles and atoms, nanophotonics, and quantum processing. Hereafter, the optical SAM-FD has been normalized to its initial peak value. It is clearly seen from Figure 4 that the SAM-FD depends on the SoP arrangements. In addition, the transverse (x - or y -) components of the SAM-FD distribution (both evanescent wave and propagating wave) break up into two peaks with opposite values. On the other hand, the z -component of the SAM-FD shape remains the Gaussian profile, as expected. The transverse (x - or y -) components of the SAM-FD are even greater than that of longitudinal (z -) component in near field but spread out quickly and fade away with the increasing

distance, as expected. When the propagation distance $z > \lambda$, the transverse (x - or y -) components of the SAM-FD can be ignored compared to the longitudinal component. Figure 5 shows that the SAM-FD profiles are different with different radial periods of initial SoP arrangement (i.e., different r_0 in this work). In particular, the transverse (x - or y -) components of the SAM-FD (both evanescent wave and propagating wave) rotate with different radial periods of initial SoP alignment due to the corresponding longitudinal components rotate with different radial periods of initial SoP arrangement.

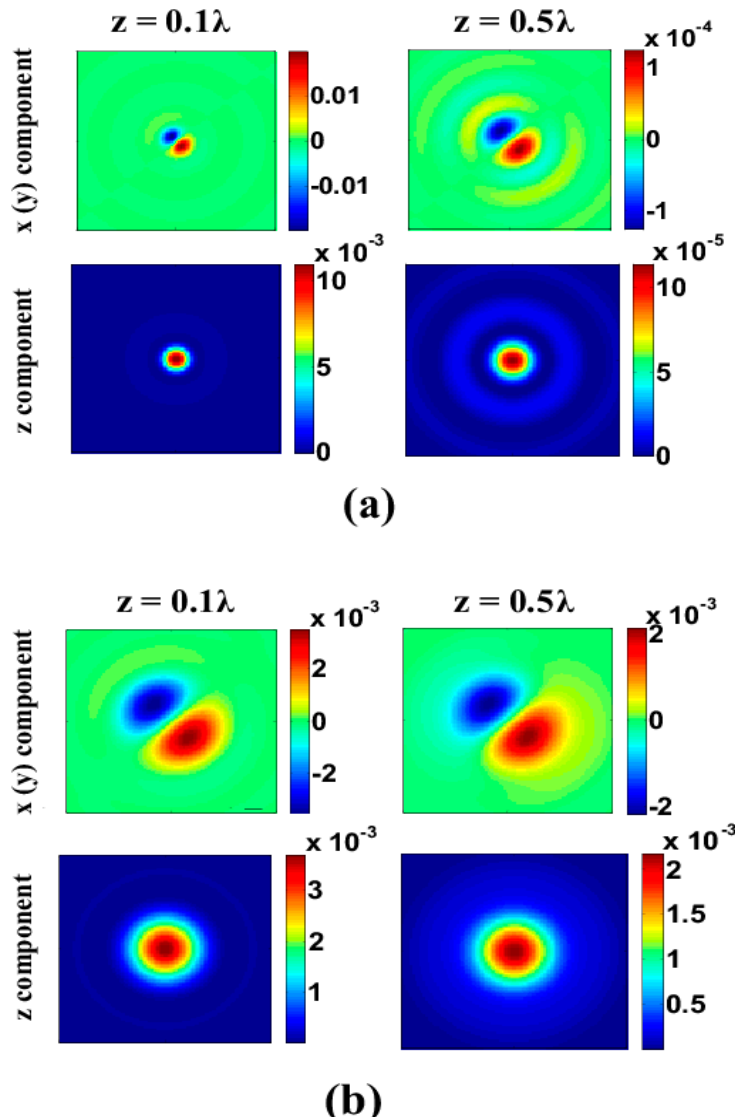


Figure 4. (Color online) The x , y , and z components of the spin angular momentum flux density (SAM-FD) of the evanescent wave and propagation wave with $w = 0.1\lambda$, $r_0 = 0.5\lambda$. Upper plots in (a,b) transverse (x - or y -) component; lower plots in (a,b) z component. All the images have the same dimension of $2 \times 2 \lambda^2$.

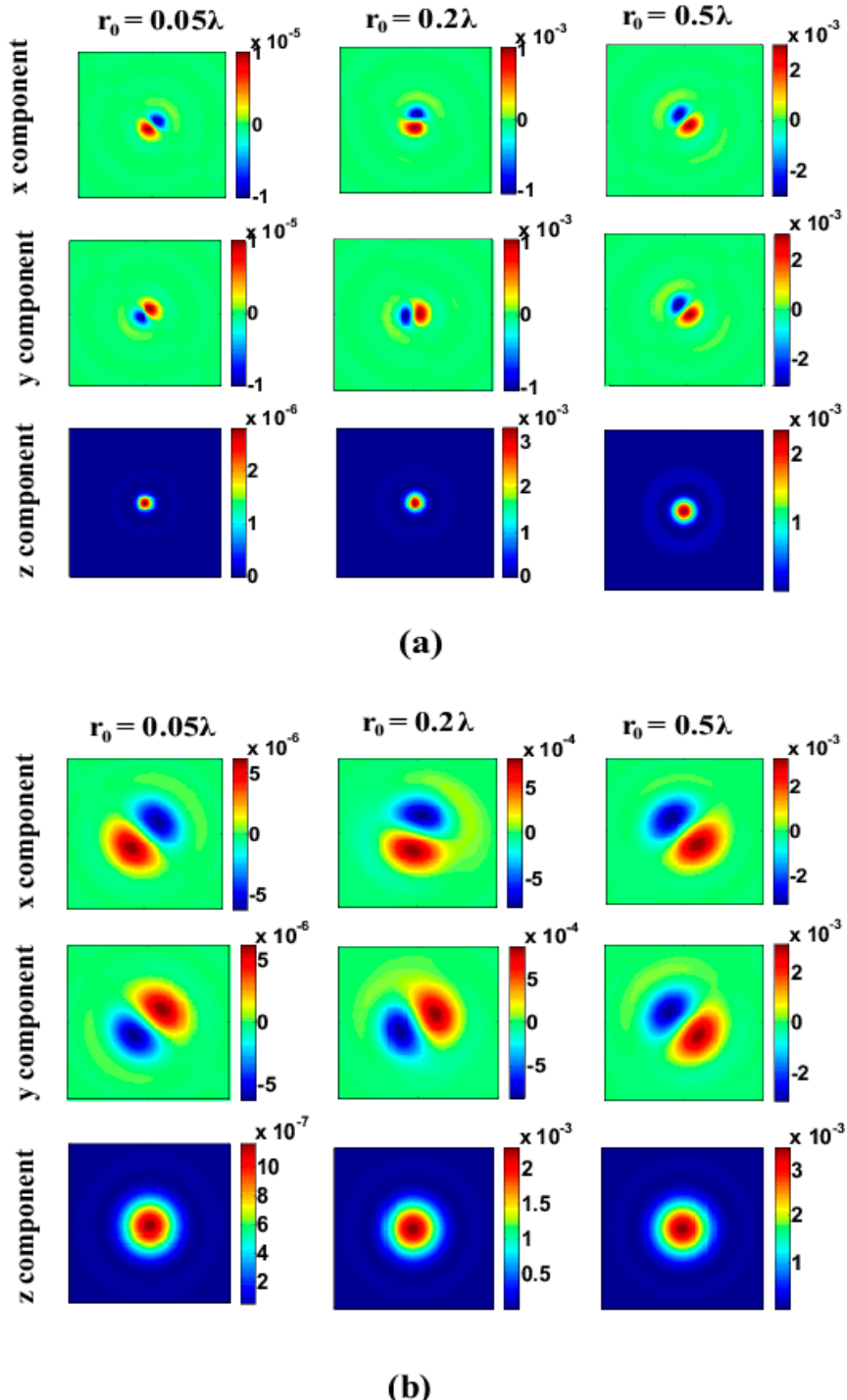


Figure 5. (Color online) The x , y , and z components of the SAM-FD of the evanescent wave and the propagating wave with $w = 0.1\lambda$, $z = 0.2\lambda$ for different radial periods of initial SoP arrangement (i.e., different r_0 in this work): (a) the evanescent wave; (b) the propagating wave. Upper plots in (a) and (b) S_x ; middle plots in (a,b) S_y ; lower plots in (a,b) S_z . All the images have the same dimension of $2 \times 2 \lambda^2$.

4. Conclusions

The near-field characteristics of the highly non-paraxial RVVB have been studied, with the comparison between the evanescent and the propagating wave parts. The longitudinal component is not negligible, and the profile is dependent on the initial SoP alignment. The profile of the longitudinal

component of a RVVB is different from that of the transverse component, leading to the variant of the total intensity pattern. The effect of the longitudinal component on the optical SAM-FD leads to a different vector structure of 3D SAM-FD. The manipulation of the 3D SAM-FD by the initial SoP arrangement may provide great potential for use in a wide variety of applications ranging from nanophotonics, quantum processing and plasmonics to biophotonics.

Author Contributions: Conceptualization, R.-P.C. and Y.G.; Methodology, R.-P.C.; Software, C.Q.; Validation, R.-P.C., Y.G. and C.Q.; Formal Analysis, L.-X.Z.; Investigation, Y.G. and C.Q.; Resources, R.-P.C.; Data Curation, C.Q.; Writing-Original Draft Preparation, Y.G. and C.Q.; Writing-Review & Editing, Y.G.; Visualization, Y.G.; Supervision, R.-P.C.; Project Administration, R.-P.C.; Funding Acquisition, R.-P.C.

Funding: This research was funded by [the National Natural Science Foundation of China] grant numbers [11574271, 11874323], [the Zhejiang Provincial Natural Science Foundation] grant number [LQ13A040001], [Zhejiang Province Welfare Technology Applied Research Project] grant number [GC19E030005].

Conflicts of Interest: The authors declare no conflict of interest.

References

- Chen, R.P.; Chen, Z.; Gao, Y.; Ding, J.; He, S. Flexible manipulation of the polarization conversions in a structured vector field in free space. *Laser Photonics Rev.* **2017**, *11*, 1700165. [[CrossRef](#)]
- Zhan, Q. Cylindrical vector beams: From mathematical concepts to applications. *Adv. Opt. Photonics* **2009**, *1*, 1–57. [[CrossRef](#)]
- Chen, R.P.; Chen, Z.; Chew, K.H.; Li, P.G.; Yu, Z.; Ding, J.; He, S. Structured caustic vector vortex optical field: Manipulating optical angular momentum flux and polarization rotation. *Sci. Rep.* **2015**, *5*, 10628. [[CrossRef](#)] [[PubMed](#)]
- Chen, R.P.; Zhong, L.X.; Chew, K.H.; Zhao, T.Y.; Zhang, X. Collapse dynamics of a vector vortex optical field with inhomogeneous states of polarization. *Laser Phys.* **2015**, *25*, 075401. [[CrossRef](#)]
- Chen, R.P.; Zhong, L.X.; Chew, K.H.; Gu, B.; Zhou, G.; Zhao, T. Effect of a spiral phase on a vector optical field with hybrid polarization states. *J. Opt.* **2015**, *17*, 065605. [[CrossRef](#)]
- Wang, X.L.; Li, Y.N.; Chen, J.; Guo, C.S.; Ding, J.P.; Wang, H.T. A new type of vector fields with hybrid states of polarization. *Opt. Express* **2010**, *18*, 10786–10795. [[CrossRef](#)] [[PubMed](#)]
- Zhan, Q.; Leger, J.R. Focus shaping using cylindrical vector beams. *Opt. Express* **2002**, *10*, 324–331. [[CrossRef](#)] [[PubMed](#)]
- Dorn, R.; Quabis, S.; Leuchs, G. Sharper focus for a radially polarized light beam. *Phys. Rev. Lett.* **2003**, *91*, 233901. [[CrossRef](#)] [[PubMed](#)]
- Ruffner, D.B.; Grier, D.G. Optical forces and torques in nonuniform beams of light. *Phys. Rev. Lett.* **2012**, *108*, 173602. [[CrossRef](#)] [[PubMed](#)]
- Chen, R.P.; Dai, C.Q. Vortex solitons of the (3 + 1)-dimensional spatially modulated cubic-quintic nonlinear Schrödinger equation with the transverse modulation. *Nonlinear Dyn.* **2017**, *90*, 1563–1570. [[CrossRef](#)]
- Chen, R.P.; Chew, K.H.; Zhou, G.; Dai, C.Q.; He, S. Vectorial effect of hybrid polarization states on the collapse dynamics of a structured optical field. *Opt. Express* **2016**, *24*, 28143. [[CrossRef](#)] [[PubMed](#)]
- Chen, R.P.; Dai, C.Q. Three-dimensional vector solitons and their stabilities in a Kerr medium with spatially inhomogeneous nonlinearity and transverse modulation. *Nonlinear Dyn.* **2017**, *88*, 2807–2816. [[CrossRef](#)]
- Chen, R.P.; Chew, K.H.; Dai, C.Q.; Zhou, G. Optical spin-to-orbital angular momentum conversion in the near field of a highly nonparaxial optical field with hybrid states of polarization. *Phys. Rev. A* **2017**, *96*, 053862. [[CrossRef](#)]
- Fornel, F.D. *Evanescent Waves: From Newtonian Optics to Atomic Optics*; Springer: Berlin, Germany, 2001.
- Agrawal, G.P.; Lax, M. Free-space wave propagation beyond the paraxial approximation. *Phys. Rev. A* **1983**, *27*, 1693–1695. [[CrossRef](#)]
- Grbic, A.; Jiang, L.; Merlin, R. Near-field plates: Subdiffraction focusing with patterned surfaces. *Science* **2008**, *320*, 511–513. [[CrossRef](#)] [[PubMed](#)]
- Merlin, R. Radiationless electromagnetic interference: Evanescent-field lenses and perfect focusing. *Science* **2007**, *317*, 927–929. [[CrossRef](#)] [[PubMed](#)]
- Lerman, G.M.; Avner, Y.; Uriel, L. Demonstration of nanofocusing by the use of plasmonic lens illuminated with radially polarized light. *Nano Lett.* **2009**, *9*, 2139–2143. [[CrossRef](#)] [[PubMed](#)]

19. Helseth, L.E. Radiationless electromagnetic interference shaping of evanescent cylindrical vector waves. *Phys. Rev. A* **2008**, *78*, 013819. [[CrossRef](#)]
20. Martínez-Herrero, R.; Mejías, P.M.; Juvells, I.; Carnicer, A. Transverse and longitudinal components of the propagating and evanescent waves associated to radially polarized nonparaxial fields. *Appl. Phys. B* **2012**, *106*, 151–159. [[CrossRef](#)]
21. Martínez-Herrero, R.; Mejías, P.M.; Carnicer, A. Evanescent field of vectorial highly non-paraxial beams. *Opt. Express* **2008**, *16*, 2845–2858. [[CrossRef](#)] [[PubMed](#)]
22. Chen, R.P.; Li, G. The evanescent wavefield part of a cylindrical vector beam. *Opt. Express* **2013**, *21*, 22246–22254. [[CrossRef](#)] [[PubMed](#)]
23. Jackson, J.D.; Levitt, L.C. Classical electrodynamics. *Phys. Today* **1999**, *52*, 78.
24. Enk, S.J.V.; Nienhuis, G. Commutation Rules and Eigenvalues of Spin and Orbital Angular Momentum of Radiation Fields. *Opt. Acta Int. J. Opt.* **1994**, *41*, 963–977.
25. Maucher, F.; Skupin, S.; Gardiner, S.A.; Hughes, I.G. Creating complex optical longitudinal polarization structures. *Phys. Rev. Lett.* **2018**, *120*, 163903. [[CrossRef](#)] [[PubMed](#)]
26. Bauer, T.; Banzer, P.; Karimi, E.; Orlov, S.; Rubano, A.; Marrucci, L.; Santamato, E.; Boyd, R.W.; Leuchs, G. Observation of optical polarization Möbius strips. *Science* **2015**, *347*, 126635. [[CrossRef](#)] [[PubMed](#)]



© 2019 by the authors. Licensee MDPI, Basel, Switzerland. This article is an open access article distributed under the terms and conditions of the Creative Commons Attribution (CC BY) license (<http://creativecommons.org/licenses/by/4.0/>).